Edge-state-mediated collective charging effects in a gate-controlled quantum dot array

Wen-Yao Wei,[1] Tung-Sheng Lo,[2] Chiu-Chun Tang,[1] Chi-Te Liang,[3] D. C. Ling,[4] C. C. Chi,[1] Chung-Yu Mou,[1] Dennis M. Newns,[5] Chang C. Tsuei,[5] and Jeng-Chung Chen[1]

[1]*Department of Physics, National Tsing-Hua University, Hsinchu 30013, Taiwan*

[2]*Institute of Physics, Academia Sinica, Taipei 115, Taiwan*

[3]*Department of Physics, National Taiwan University, Taipei 106, Taiwan*

[4]*Department of Physics, Tamkang University, Tamsui District, New Taipei City 25137, Taiwan*

[5]*IBM Thomas J. Watson Research Center, Yorktown Heights, New York 10598, USA*

(Received 27 March 2016; revised manuscript received 8 March 2017; published 25 April 2017)

We report the observation of two distinct types of magnetoconductance oscillations in six coupled quantum dots (QDs) in the integer quantum Hall regime. By tuning the magnetic field and gate voltage, we find robust conductance peaks and dips on the plateau of one conductance quantum $2e^2/h$. These features fall into two types associated with two different collective quantum states: for the first type, only dips and the crossing behaviors are found, and their traces show an anomalous temperature dependence, named "reversed Coulomb blockade oscillation", whereas for the second type, the peak traces show both crossing and anticrossing behaviors with resonance-type temperature dependence. Notably, all peaks show clear Coulomb diamonds in their differential conductance. We argue that the observed features reveal the electron addition spectra in an edge-state-mediated QD network, manifesting intricate interdot and dot-edge Coulomb interactions. In the first-type regime, the dots are more isolated from each other and the electron transport is governed by the dot-edge interaction. Conversely, in the second-type regime, the QDs behave as a coupled dot array due to the presence of strong interdot interactions. Our results open a route by using the edge-state-mediated multi-QD system as a laboratory for exploring coherent many-body interactions.

DOI: 10.1103/PhysRevB.95.155445

I. INTRODUCTION

One-dimensional chiral edge states can be constructed in a GaAs two-dimensional electron gas (2DEG) in the integer quantum Hall (IQH) regime [1] wherein IQH states in the vicinity of the edges of the sample spatially separate into alternating strips of incompressible and compressible states [2–4]. Each edge state is associated with an extended compressible region with one fully occupied Landau level (LL), and follows the equipotential along the sample border. The number n of the edge states counts the number of the fully occupied Landau levels (LLs) in the bulk and corresponds to the quantized plateau of the Hall conductance at $n(e^2/h)$. Theoretically, n can be understood as a topological quantum number, i.e., the Chern number [5]. Due to the protection of the topological invariant, the edge states are intrinsically immune to environmental disorders. Numerous studies on 2DEGs in the IQH regime have experimentally demonstrated that the edge states possess rather long coherence length [6–9], and thus provide a playground for coherently probing the quantum states in a device.

In mesoscopic devices, the edge states can interact with nearby local charge states and give rise to various resonant transmission and reflection interference on the conductance G [10,11]. The selective manipulation and detection of the edge channels were first observed by using the point contacts [12]. The population of the edge states is manipulated either by adjusting the local potential via the external gate voltages V_g or by applying the magnetic field B to alter the occupations of LLs. Conductance variations can be understood by the Landauer-Büttiker formalism [13]. Subsequent studies are divided into two branches: the investigation of magnetoresistance in quantum dot (QD) and quantum antidot (QAD) systems.

A quantum dot is an electron droplet confined in a nanoscale region, wherein both the energy and charges are quantized. In the IQH regime, the formation of LLs leads to a modulation of the screening properties of the electrons in the dot, yielding the divisions of electrons into compressible and incompressible regions [14,15]. Conductance measurements are commonly used to manifest the addition spectra of the QD system [12,14–23]. As $G < 2e^2/h$ ($\equiv G_0$), electrons are confined in explicit charge states and the electron transport is dominated by Coulomb interactions. For example, in a fairly large QD, containing nearly hundreds of electrons with a filling factor ν larger than or close to 2, the lowest (LL0) and the first orbital (LL1) LLs form a compressible metallic outer ring and inner core islands, respectively, which are separated by insulating incompressible regions. Conductance is regulated by a mixture of the Coulomb blockade (CB) between electrons in the localized outer ring with LL0 and inner core electrons with LL1. As a result, it reveals periodic CB oscillations with modulated peak separation and amplitude associated with noncyclical depopulation of LLs [12,14–23]. Robust interference phenomena emerge when $G > G_0$. They arise as the confining potential of the QDs becomes relatively shallower, so the outer edge states can extend through the QDs. The fully transmitted edge channels interact with the trapped core electrons, leading to interference [12,17]. Furthermore, the interplay between interference and interaction gives rise to distinct Aharonov-Bohm type oscillations in conductance [12,24,25].

The quantum antidot (QAD) is a small potential hill, where the electron is repelled, rather than attracted by a trap potential as in the QD [11,26,27]. In the IQH regime, the edge states are established along the periphery of the potential hill and circulate as closed chiral orbits. The localized

orbits then interact with the extended edge channels along the boundary of the 2DEG. Various fascinating phenomena associated with the effects of resonant transmission, reflection, and the electron-electron (e-e) interactions have been studied, including resonant peak or dip structures on the quantized plateau [28,29], Aharonov-Bohm oscillations of conductance [26,30,31], charge rigidity (quantization) [32], spectator modes in antidot molecules [33], the Kondo-like zero-bias anomaly [34], and charging effects [35].

Based on the aforementioned findings, the QD and QAD devices in the IQH regime are known to be an ideal tool for investigating various interference and Coulomb interaction effects [36,37]. For a multi-QD/multi-QAD system, the interactions among the dots/antidots and the edge states provide a platform to investigate various many-body physics, but this scheme has not been fully explored to date. To this end, we report the observation of edge-state-mediated collective charging effects in a quantum dot array (QDA). A variety of coherent many-body states is observed. These states mimicking the bonding states in an artificial molecule are explicitly probed by conductance spectra and can be manipulated by tuning the interdot coupling through gate voltages and magnetic fields.

II. EXPERIMENTAL DESIGN

Our experimental design is schematically illustrated in Fig. 1. The QDA is formed by confining the 2DEG to a chain of six quantum dots (QDs) via biasing negative voltages V_M and V_g on the surface side gate and the corrugated gate, respectively [see the SEM image of the device shown in the upper panel of Fig. 1(a)]. Under high magnetic field B, the electron states fall into the IQH region. Conforming to the filling factor ν

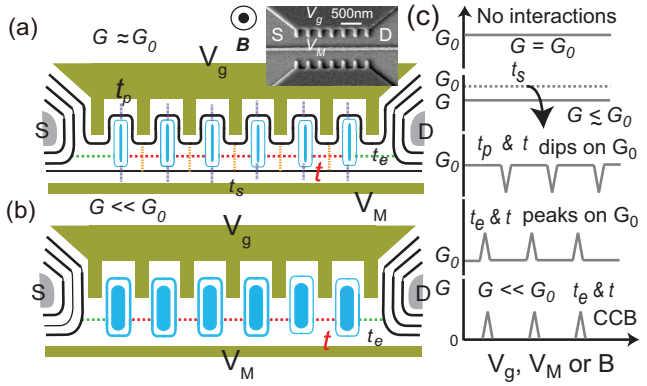

FIG. 1. A schematic top view of the QDA device in the IQH regime. The QDA consists of the blue stadium-shaped cores and the outer rings, which are localized compressible (metallic) states. (a) In the case of $G \approx G_0$, one edge channel flows along the device boundaries and extends into the leads. Various possible tunneling paths are indicated by the colored dashed lines. (b) In the case of $G \ll G_0$, the extended edge state disappears; consequently, all states are localized in the dots. The electron transport is dominated by the interdot coupling strength. (c) The symbolic change of the conductance induced by different interacting paths as a function of gate voltages or B (see the text for the details). The upper-right inset in (a) displays a scanning electron microscope (SEM) image of the device defined on the top surface of a GaAs/AlGaAs heterostructure.

of LLs and the potential profile, electrons confined within the regions between two gates self-consistently tuck into stadium islands with a partially filled LL, surrounded by alternating compressible conducting and incompressible insulating stripes with fully occupied LLs [16]. The outermost compressible electrons can either flow along the edge of the confining potential and extend to the 2DEG, as shown in Fig. 1(a), or fold into closed orbits as nominally isolated dots or rings, as shown in Fig. 1(b) [17]. In addition, we consider a pair of opposite spin-degenerate edge states propagating along the periphery of the confining potential.

The correlated interactions between the dots and the edge states are indicated by the colored dashed lines in Figs. 1(a) and 1(b), including (i) the interdot tunneling with amplitude t (red horizontal lines), (ii) the tunneling between each individual dot and the outer extended edge states with amplitude t_p (blue vertical lines), (iii) the tunneling between the two end dots and the edge states on the source (S) and drain (D) leads with amplitude t_e (green horizontal lines), and (iv) the tunneling between two opposite extended edge states with amplitude t_s (orange vertical lines). Here, we simply apply comprehensive understandings of single-QD/single-QAD systems in the IQH regime, as reported earlier [23,29,31,36], and extend them to the case of a multidot system. Note that different tunneling paths exhibit their own distinct conductance G characters, as displayed in Fig. 1(c). In the absence of tunneling, one would expect a quantized G at $2e^2/h$ ($\equiv G_0$) to be observed in an isolated QDA. The interedge coupling t_s induces backscattering between the two opposite-flow edges and causes G to be less than G_0. The dot-edge coupling t_p occurs whenever the Coulomb blockade (CB) is removed and produces periodic dips on G_0 associated with the tuning parameter B, V_M, and V_g. Conversely, as the two end dots are coupled to the reflected edge state on the S and D leads via t_e, extra accessible conductance can contribute to G; consequently, the CB-type peaks emerge on the G_0 plateau. Figure 1(b) depicts the case of $G \ll G_0$ in which the extended edge channel vanishes in the array area. Under this circumstance, a serially coupled QD chain is established through the assistance of t, and the transport is dominated by collective CB (CCB) phenomena [38]. These aforementioned interactions can be controlled by adjusting the potential profile via tuning V_g and V_M or by varying the electronic states of the QDs without modifying the potential landscape via tuning B. At a given V_g, for example, a less negative V_M lowers the tunneling barrier, hence increasing t and t_e. Alternatively, by altering B, both t and t_e will change with the filling of the LLs of the QDs. We therefore adjust (V_g, V_M) and B to explore accessible states of the QDA in the following studies.

The QDA device was implemented by using a pair of metallic gates on top of a GaAs/AlGaAs heterostructure with 2DEG 80 nm beneath the surface. The carrier density of the 2DEG is $n_s = 3.4 \times 10^{11}$ cm^{-2}, and the mobility is $\mu = 8.8 \times 10^5$ cm^2/V s at 4.2 K, corresponding to a transport mean-free path of $\sim$8.4 μm. The QDA was patterned by standard e-beam lithography and was electrostatically defined by applying negative voltages on two metallic Au/Cr gates. The device consists of a sequence of six quantum dots. The upper-right inset of Fig. 1(a) displays the scanning electron microscope image of the QDA device. We label the side-gate

voltage as V_g and the middle-gate voltage as V_M. The protruding fingers on the side gate have a period of 250 nm, and V_g is mainly used to define the potential around the fingers. The measurements were performed in a dilution refrigerator with a base temperature T of 20 mK. A standard lock-in technique with ac excitation voltage $V_{\rm rms} = 10$ μV at a frequency of 17 Hz was employed. A magnetic field B was applied perpendicularly to the plane of the QDA.

III. RESULTS AND DISCUSSION

To illustrate the characteristics of the QDA device with the scan of the gate voltages, Fig. 2(a) shows the representative G traces versus V_M with V_g at -0.36 V, -0.42 V, -0.47 V, -0.52 V, and -0.61 V for $B = 1.88$ T. Conductance plateaus at approximately G_0 and $2G_0$ are readily observed, suggesting the edge-state nature of electron transport. The value of the first plateau slightly deviates from G_0 by $\sim$2%, suggesting that t_s is relatively weak. The plateau features are evident when B exceeds 1.4 T ($\nu \sim$ 6–8 in 2DEG), indicating the important role of the QH edge states. As B ranges from 1.4 T to 2.8 T,

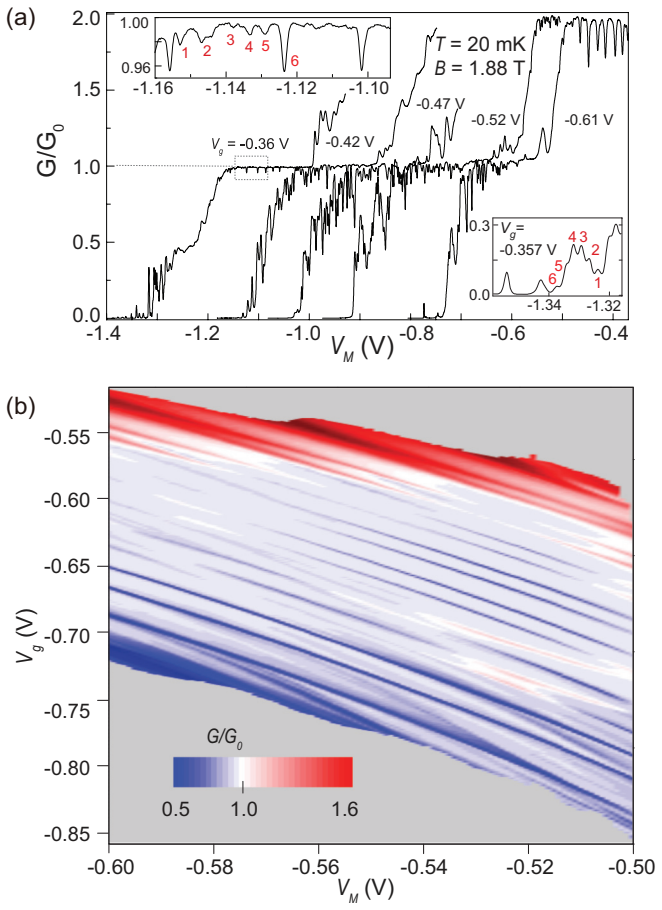

FIG. 2. (a) Normalized conductance G/G_0 as a function of V_M with a few selected side-gate voltages V_g at $B = 1.88$ T and $T = 22$ mK. The upper-left and lower-right insets show the enlarged view of the dip structures on the first plateau at $V_g = -0.36$ V and the CB peaks at $V_g = -0.357$ V, respectively. (b) Conductance map $G/G_0(V_g, V_M)$ on the first plateau. Note that the white background indicates G_0, and the red and blue traces correspond to peaks and dips above and below G_0, respectively.

various dip and peak structures are superimposed onto the G_0 plateau and evolve with (V_g, V_M), manifesting the intriguing interplay of t_p, t, and t_e and corresponding with the tunneling events described in Fig. 1(c). All the dip and peak structures are strikingly reproducible, and similar features are observed in all studied devices.

The upper-left inset of Fig. 2(a) shows the observation of five smaller oscillations between two key downward peaks. Similar features have been reported on a spin-resolved plateau of e^2/h in a QDA, and are attributed to the formation of minibands [39]. In this work, we argue that the observed dips originate from the charging effect between the QDs and the edge states (see below). As $G \ll G_0$, the dots are tunneling-coupled in series, and periodic CB-type peaks are present. At specific gate voltages, where t is comparatively large, six minipeaks appear on a single broad peak, as shown in the lower-right inset of Fig. 2(a). The emergence of the well-resolved six minipeaks strongly suggests that the six quantum dots are collectively coupled and, more importantly, demonstrates the existence of a fair uniformity of the dot array [40]. However, it is difficult to individually control a specific dot in the array by merely using two gates; as a result, the number of electrons in each dot may vary from one dot to another due to the presence of inevitable disorders. An extensive study on the CB-related physics under the conditions of $G < G_0$ will be presented elsewhere [41]. The present work focuses on elucidating the coupling effects between the dots and the edge states in the case of $G \geqslant G_0$, as illustrated in Fig. 1(a).

We adopt an empirical rule from an early study on a similar GaAs-based quantum dot that the carrier density of the dot is approximately 0.7 times smaller than that of the 2DEG confined in a GaAs/AlGaAs heterostructure [23]. Correspondingly, the deduced filling factor in the studied array is estimated to be four to six ($2 \sim 3$ occupied spin-degenerate LLs). Therefore, we can reasonably infer that the quantum dot array consists of a pair of fully transmitted edge channels plus isolated inner cores and outer rings, similar to the configuration in early studies [23,29]. Under such circumstance, both inter- and intra-LL scatterings are present and our proposed scenario illustrated in Fig. 1(a) is realized. More importantly, there are extra advantages to operate the QDA device in this regime: the Fermi level in the bulk 2DEG is approximately independent of magnetic field and the absence of spin-flip scattering makes it possible to attribute G mainly from a spin-degenerate edge channel [29].

Figure 2(b) shows a comprehensive G plot of the dip (the blue trace) and the peak (the red trace) on the G_0 plateau (the white background) as a function of V_g and V_M. As mentioned earlier, although the QDs in the array were fabricated to be nominally identical, the shape of the confinement potential of each dot is unavoidably different due to disorders in the wafer, imperfections in the lithography process, and the limited tunability of two gate voltages. The fact that these dip/peak features strongly depend on their locations in the V_M-V_g plane represents the variations of the confinement potential; therefore, the loci of the dips/peaks manifest as a "fingerprint" of a particular configuration of the QDs. By closely following these traces, we can see that a blue trace can evolve into a red one at a certain value of (V_M, V_g), and two such traces exhibit an anticrossing-like behavior; e.g., see the traces in the vicinity of $(V_M, V_g) \sim (-0.52, -0.73)$ V. In a certain

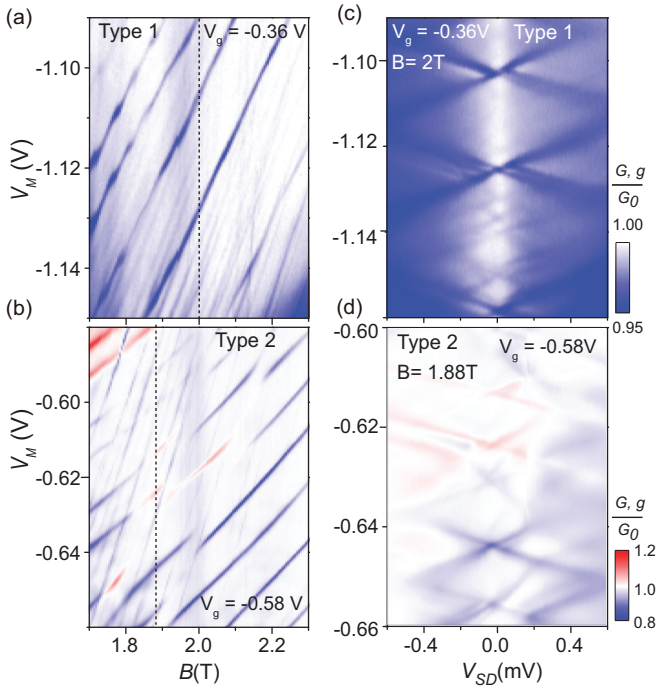

FIG. 3. The conductance spectrum displayed by the V_M vs B plot for (a) type 1 with fixed $V_g = -0.36$ V, and for (b) type 2 with fixed $V_g = -0.58$ V. The color-scale plot of $dI/dV_{\rm SD}$ as a function of V_M and the source-drain voltage $V_{\rm SD}$ for (c) type 1 with fixed $V_g = -0.36$ V and $B = 2$ T, and for (d) type 2 with fixed $V_g = -0.58$ V and $B = 1.88$ T.

regime, however, only the dip—the blue traces—can be found, and the traces exclusively show crossing behaviors, e.g., in the lower part of Fig. 2(b) near the end of the plateau. The observation of the peaks and dips on G_0 is in accordance with our suggestion that interactions between the dots and the edge channels induce intriguing resonant transmission and reflection in the form of the CB-type charging effect. In light of these findings, the conductance map shown in Fig. 2(b) can be viewed as a charge stability diagram of the QDA, which reveals the evolution of the energy levels formed in the QDA with tuning (V_M, V_g). As elucidated by early studies on a double-quantum-dot system, the crossing traces indicate that each dot retains its own electronic states, i.e., in the weak-t regime, whereas the anticrossing trace signals the formation of coherent bonding/antibonding states arising from the formation of coupled dots [42]. The appearance of the peak feature along with the anticrossing trace convincingly indicates that a fairly strong t is present. We thereby classify the conductance into two types: type 1 refers to G features in the weak-t regime where only dips—the blue traces—are found, and type 2 to those in the strong-t regime, where both the peak and dip traces are observed. We will show more comprehensive data below to support our claim.

Figures 3(a) and 3(b) show the conductance spectrum tuned by V_M and B at a fixed gate voltage V_g for type 1 and type 2, respectively. Here we apply the gate voltages for type 1 such that the deeper and the minor dips are both visible; e.g., see the upper-left inset of Fig. 2(a). The B-V_M plot of the G spectrum reveals two distinct features. First, the peak or dip traces in both types exhibit positive dV_M/dB slopes, suggesting that increasing B is equivalent to applying less negative voltages to the device. Recent studies on quantum Hall interferometers have demonstrated that the positive dV_M/dB slope arises from charging effects [36,43], in strong contrast to the negative one from the interference effect [43]. It supports that the dip and the peak structures with positive dV_M/dB slopes indeed originate from interactions between the dots and the edge states. Second, the anticrossing behaviors are observable for these type-2 traces; in contrast, only the crossing behavior can be found for those type-1 ones. Note that the anticrossing traces in the stability diagram spanned by V_M and B and those observed in the V_M-V_g plane shown in Fig. 2(b) are both predominated by the effect of t. The distinct signatures in the conductance spectrum for type 1 and type 2 are consistently observed in the V_M-V_g and B-V_M plots, strongly suggesting that type 1 and type 2 represent different collective quantum states with different values of t in the dot array. For type 1, the six dots are weakly coupled, i.e., $t \sim 0$, and are also coupled to edge channels via t_p. Each tunneling process between an individual dot and the edge states gives rise to a dip structure. In contrast, the six dots are strongly coupled for type 2, where the dip and the peak structures are attributed to the coherent tunneling events between the molecule-like bound states and the edge states, governed by the interplay of t, t_p, and t_e.

To substantiate the above-described scenarios, Figs. 3(c) and 3(d) show the differential conductance g $(=dI/dV_{\rm SD})$ in the V_M-$V_{\rm SD}$ plot for type 1 and type 2, respectively. Both the peaks and the dips exhibit pronounced Coulomb-diamond structures, providing compelling evidence for the predominant role played by Coulomb charging effects. The dips in type 1 show "inverted" diamonds, i.e., lower g at the diamond boundaries [see Fig. 3(c)]. In addition, fine structures are visible and skirt along the diamond borders, which manifest the tunneling spectrum of the excited charge states. More interestingly, an intriguing nested diamond structure, i.e., small diamonds from the minor dips enclosed by large diamonds from the deeper dips, is also found in type 1. Figures 4(a) and 4(b) show the V_M dependence of G at different temperatures for type 1 and type 2, respectively. For type 1, two major dips at $V_M \sim -1.13$ V and -1.10 V are observed. The amplitude of the dips slightly varies with the increase of temperature to 1 K, whereas the width of the dips increases and the plateau value slightly decreases. The temperature dependence of the dip conductance can be qualitatively described by $G \sim G_0 - G_{CB}(T)$, where $G_{CB}(T)$ represents the typical temperature dependence of CB for a single QD [44]. For type 2, both dip and peak amplitudes monotonically decrease with increasing T, indicating that the increase of T thermally smears out the effects of t, t_p, and t_e. The different temperature dependencies of the dip features observed for type 1 and type 2 unambiguously support that they are attributed to different quantum states.

We proceed to estimate some relevant parameters of the studied QDA. Based on the voltage bias spectroscopy shown in Fig. 3(c), we evaluate the charging energy $U = e^2/C \sim 1.0$ to 0.8 meV from the variations of the diamond width, where the total QD capacitance C is estimated to be approximately 130 aF. As shown in Fig. 4(a), the dip spacing between the two pronounced dips is $\Delta V_M = e/C_M \sim 30$ mV ($C_M \sim 5$ aF; see below for details). The slope of the dip trace is approximately

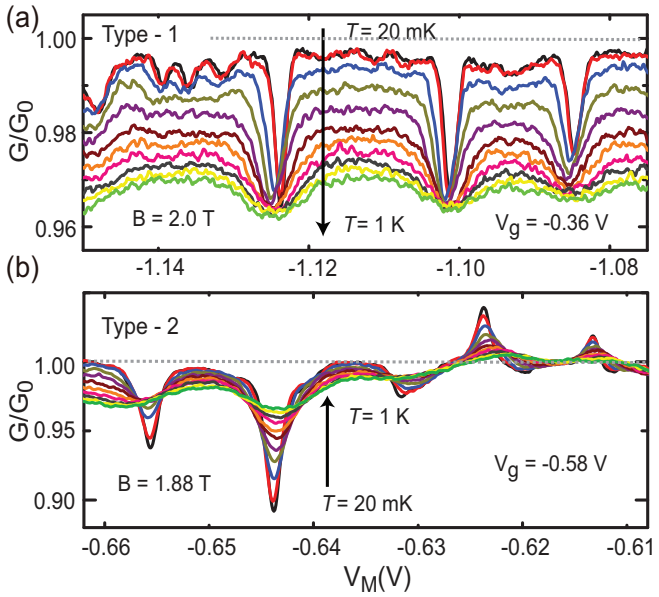

FIG. 4. The features of V_M-dependent conductance for (a) type 1 and (b) type 2 show distinctly different temperature dependence. The data in (a) and (b) were extracted from the dashed lines shown in Figs. 3(a) and 3(b), respectively.

$dV_M/dB = 0.2$ V/T extracted from Fig. 3(a). We adopt the approach in Ref. [36] to obtain $dV_M/dB = e\nu_{\rm dot}A_{\rm dot}/C_M\Phi_0$, where Φ_0 is a flux quantum, $\nu_{\rm dot}$ is the number of occupied LLs in a dot, and $A_{\rm dot}$ is the area of a dot. By assuming $\nu_{\rm dot} \sim 2$ at $B = 2$ T, we extract $A_{\rm dot} \sim 1 \times 10^{-14}$ m^2, which is consistent with the size of a stadium dot evaluated from the SEM image of the device after subtracting a depletion length ~75 nm. Theoretically, t in a QDA can be approximately scaled as $t \sim \hbar^2/m^*d^2$, where m^* is the effective mass of GaAs and d is the mean size of a dot [38]. In our case, t is approximately 0.1 meV with $d \sim 100$ nm. The values of t_p, t_e, and t_s are expected to lie within the same order of magnitude as that of t.

IV. SIMULATION OF CHARGE TRANSPORT IN THE WEAK-COUPLING REGIME

It is difficult for us to perform a fully quantitative analysis of our data without specific knowledge of t, t_p, and t_e as a function of the microscopic parameters of the dots. Nevertheless, we attempt to estimate the relevant parameters of the QDA in terms of the capacitance model, which is more appropriate to describe the conditions of the QDs in the type-1 regime, where each dot is nearly isolated [42]. This classical description, known as a "constant interaction model", may not be very applicable to the type-2 regime, where t is relatively strong; strictly speaking, one needs to deliberate the complicated effects of the e-e interactions [38,41,44,45].

Data analysis suggests that the dots in type 1 are weakly coupled to each other. To provide a self-consistent check, we calculate the charge stability diagram of the QDA based on this scenario. Here we simply combine the approaches proposed by Refs. [36] and [15] in the multiple-quantum-dot

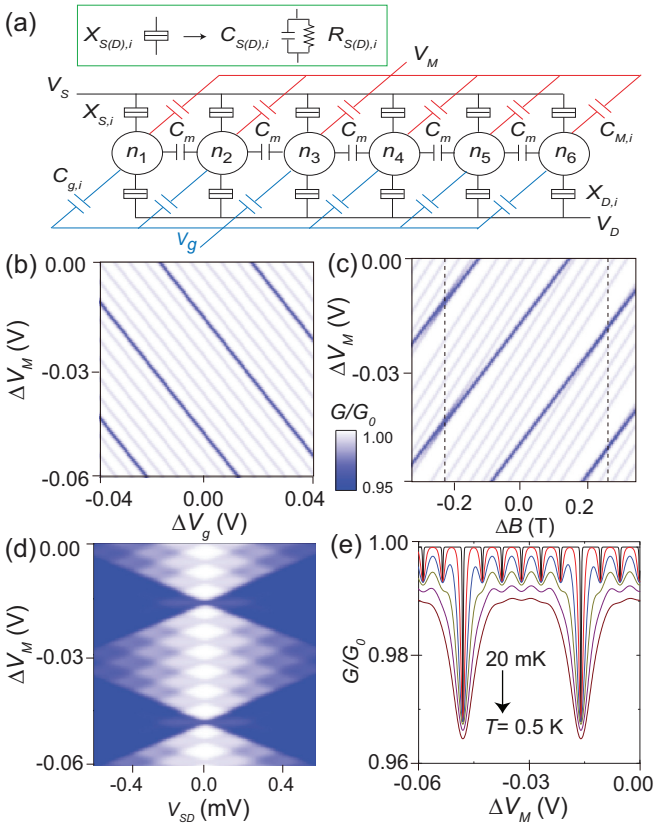

FIG. 5. Simulation results of a collective charge transport for a six-quantum-dot array in type 1 described in the text. (a) The QDA is modeled by a network of tunnel junctions and capacitors. The inset shows the equivalent circuit of the tunnel barriers. (b) The conductance as a function of ΔV_M and ΔV_g maps out the charge stability diagram of the QDA. (c) The ΔV_M-B plot of conductance. The dashed lines mark ΔB at which the darker and lighter traces intersect. (d) The ΔV_M-$V_{\rm SD}$ plot of differential conductance $dI/dV_{\rm SD}$, which shows inverted Coulomb diamond structures. (e) The temperature dependence of G as a function of ΔV_M at $T = 20$, 100, 200, 300, 400, 500 mK.

system by including the interdot interactions. Figure 5 shows a schematic diagram of the model for the QDA with the upper and lower tunneling junctions to the edges. The upper/lower edge states carrying currents are in equilibrium with the source/drain contact and have a quasi-Fermi energy equal to μ_S/μ_D $(=eV_S/eV_D)$ [46]. We use a small capacitor C_m to phenomenologically account for the weak interdot coupling t. Each dot is capacitively coupled to the middle/side gate with voltage V_M/V_g through a capacitor C_M/C_g. We ignore the cross capacitance between the middle and the side gates. The inset of Fig. 5(a) shows the equivalent circuit of a tunnel junction of the ith dot to the edge upper (lower) channel, characterized by a capacitor $C_i^{S(D)}$ and a resistor $R_i^{S(D)}$. The number of electrons in the ith dot is n_i. As the magnetic field ranges from 1.4 T to 2.8 T, the electrons of the dot in the quantum Hall states are distributed into an outer ring and an inner core with the different LLs. To simplify this model without losing the most essential features, we consider that each QD comprises one core. The charges q_i in the ith dot can

be written as [42]

$$\begin{aligned} q_1 &= C_S^1(V_1 - V_S) + C_M(V_1 - V_M) + C_m(V_1 - V_2) \\ &\quad + C_D^1(V_1 - V_D), \\ q_2 &= C_S^1(V_2 - V_S) + C_M(V_2 - V_M) + C_m(V_2 - V_1) \\ &\quad + C_m(V_2 - V_3) + C_D^2(V_2 - V_D), \\ &\cdots, \\ q_6 &= C_S^1(V_6 - V_S) + C_M(V_6 - V_M) + C_m(V_6 - V_5) \\ &\quad + C_D^6(V_6 - V_D). \end{aligned} \tag{1}$$

The values of q_i vary with the flux changes. Here, we adopt the approach in Ref. [36] by considering

$$q_i = -n_i|e| + \nu_{\rm dot}\frac{\delta B A_i}{\Phi_0}|e|, \tag{2}$$

where $\nu_{\rm dot} \sim 2$ is the occupied LL in the dot, A_i is the area of the ith dot, and δB is the variation of the magnetic field. The total charge Q can be expressed in a matrix form $\hat{Q} = \hat{C} \cdot \hat{V}$ [42], where $\hat{Q} = [q_1, q_2, \ldots, q_6]$, $\hat{V} = [V_1, V_2, \ldots, V_6]$, and $\hat{C}$ is the matrix of the capacitor network. For a given charge configuration n_i of the quantum dots, the electrostatic energy E_{n_i} can be obtained by $E_{n_i} = \frac{1}{2}\hat{Q} \cdot \hat{C}^{-1} \cdot \hat{Q}$. In the linear transport regime, i.e., $V_S \sim V_D \sim 0$, the charging energy for n_i to $n_i \pm 1$ can be obtained from $\Delta E_{n_i} = E_{n_i} - E_{n_i \pm 1}$.

The removing of the CB in the dots causes the interedge scatterings. Consequently, it results in a dip on the plateau. Therefore, the conductance can be described as $G = 2e^2/h - G_{CB}$, where G_{CB} is the conductance of CB oscillations. It has been reported that G_{CB} can be derived from $I_{CB}(V_{\rm SD})$ characteristics of the dots [47]:

$$I_{CB} = e\sum_{n_i}\sum_{i=1}^{6}[\Gamma_{i\longrightarrow S} - \Gamma_{S\longrightarrow i}]P_{\{n_i\}}. \tag{3}$$

Here $P_{\{n_i\}}$ denotes the probability of finding n_i in the dots. The notation $\Gamma_{i\to S}$ is the transition rate of tunneling an electron from the ith dot to the source or vice versa, and can be expressed as

$$\Gamma_{i\to S} = \frac{1}{e^2 R_i^S}\frac{-\Delta E_{\{n_i\}}}{1 - \exp(\Delta E_{\{n_i\}}/k_B T)}. \tag{4}$$

We follow the procedures discussed in Chapter 3 of Ref. [47] to obtain $P_{\{n_i\}}$ and calculate the nonlinear transport of the QDA. The relevant parameters adopted in the following are either estimated from the data by standard methods for characterizing a quantum dot or chosen to match the experimental data. We have $C_i^S \sim C_i^D \sim 90$ aF, $C_g \sim C_M \sim 5$ aF, $C_m \sim 5$ aF, $R_i^S \sim R_i^D \sim 500$ kΩ, $A_i \sim 10^{-14}$ m^2 for $i = 1$ to 5, and $R_6^S \sim R_6^D \sim 100$ kΩ, $A_6 \sim 8.5 \times 10^{-15}$ m^2 for the sixth dot. Note that we consider the sixth dot as a variant dot with a smaller tunneling barrier to the edges and put about $0.17e$ offset charges between adjacent dots to account for the charge variations among the dots.

Figures 5(b) to 5(e) show the simulation results. The darker blue lines trace the deeper dips arising from the sixth dot which has a stronger coupling to the edges. The lighter traces are from the smaller dips attributed to the rest of normal dots. Figure 5(b) shows the calculated conductance as a function of ΔV_g and ΔV_M, which maps out the charge stability diagram of the QDA. Figure 5(c) shows the ΔV_M-B plot of G. As indicated by the dashed lines in Fig. 5(c), the deeper and lighter traces intersect at a specific B, which is in good agreement with the data shown in Fig. 3(a). The constant slope of the intersecting traces indicates a weak interdot coupling t among the dots. Figure 5(d) shows the differential conductance $dI/dV_{\rm SD}$ plot as a function of ΔV_M and $V_{\rm SD}$. We can find "inverted" Coulomb diamonds; i.e., the diamond borders indicate lower conductance as CB is removed. Moreover, the diamonds show nested features: small diamonds associated with the small oscillations are enclosed by a large diamond from the variant dot. The stimulated temperature dependence of the dip conductance is shown in Fig. 5(e). Notably, turning the G traces upside down, the T dependence of the dip features manifests typical CB behavior of the QD (see, e.g., Fig. 2 in Ref. [44]). The reduction of the plateau value with the increase of T is a consequence of increasing the interedge scattering from the normal dots. Our simple model can quantitatively reconcile the main features observed in type 1 and support our arguments: (i) the dots are weakly coupled to each other, and (ii) the dip features are induced by the edge-channel-mediated CB oscillations. By modeling the QDA as a network of tunnel junctions and capacitors, we suggest that a variant dot with a smaller tunneling barrier is responsible for the deeper dip. The discrepancies in smaller dips can be reconciled when more specific conditions are considered.

V. CONCLUSION

In summary, we have presented evidence for quantum Hall edge-state-mediated collective charging effects in a QDA on the plateau of one conductance quantum G_0. Through a combination of applying magnetic fields and gate voltages, the electron density of the dots and the interdot coupling can be continuously fine-tuned to enable the QDA conductance spectrum to undergo a localization-to-delocalization transition process. In the weak-coupling regime, electrons are localized in individual dots. The tunneling between the edge states and a single dot produces periodic dip structures on G_0 when the CB of one dot is removed. With increasing coherent interdot coupling, the electrons can be delocalized among the dots. The interplay of the interactions between the QDA and the edge states gives rise to intertwined dip and peak features on G_0. Our results demonstrate that the edge channel can be utilized to manipulate and probe the collective charge states in an interacting quantum-dot system. The QDA-edge channel network could potentially serve as an on-chip laboratory for investigating many-body interactions.

ACKNOWLEDGMENTS

We thank Kuan-Ting Lin for his experimental assistance and fruitful discussions on the experiment. This work was supported by the Ministry of Science and Technology of Taiwan under Grants No. NSC 101-2628-M-007-002-MY3, No. NSC 102-2112-M-032-005-MY3, and MOST 104-2112-M-007-010-MY3.

[1] R. E. Prange and S. M. Girvin, *The Quantum Hall Effect* (Springer, Berlin, 1987).

[2] B. I. Halperin, Phys. Rev. B **25**, 2185 (1982).

[3] D. B. Chklovskii, B. I. Shklovskii, and L. I. Glazman, Phys. Rev. B **46**, 4026 (1992).

[4] B. Y. Gelfand and B. I. Halperin, Phys. Rev. B **49**, 1862 (1994).

[5] D. J. Thouless, M. Kohmoto, M. P. Nightingale, and M. den Nijs, Phys. Rev. Lett. **49**, 405 (1982).

[6] B. J. van Wees, E. M. M. Willems, L. P. Kouwenhoven, C. J. P. M. Harmans, J. G. Williamson, C. T. Foxon, and J. J. Harris, Phys. Rev. B **39**, 8066 (1989).

[7] S. Komiyama, H. Hirai, S. Sasa, and S. Hiyamizu, Phys. Rev. B **40**, 12566 (1989).

[8] B. W. Alphenaar, P. L. McEuen, R. G. Wheeler, and R. N. Sacks, Phys. Rev. Lett. **64**, 677 (1990).

[9] P. Roulleau, F. Portier, P. Roche, A. Cavanna, G. Faini, U. Gennser, and D. Mailly, Phys. Rev. Lett. **100**, 126802 (2008).

[10] L. L. Sohn, L. P. Kouwenhoven, and G. Schön, *Mesoscopic Electron Transport* (Kluwer Academic Publishers, Dordrecht, 1997).

[11] H.-S. Sim, M. Kataoka, and C. J. B. Ford, Phys. Rep. **456**, 127 (2008).

[12] B. J. van Wees, E. M. M. Willems, C. J. P. M. Harmans, C. W. J. Beenakker, H. van Houten, J. G. Williamson, C. T. Foxon, and J. J. Harris, Phys. Rev. Lett. **62**, 1181 (1989).

[13] M. Büttiker, Phys. Rev. Lett. **57**, 1761 (1986).

[14] I. K. Marmorkos and C. W. J. Beenakker, Phys. Rev. B **46**, 15562 (1992).

[15] A. K. Evans, L. I. Glazman, and B. I. Shklovskii, Phys. Rev. B **48**, 11120 (1993).

[16] P. L. McEuen, E. B. Foxman, J. Kinaret, U. Meirav, M. A. Kastner, N. S. Wingreen, and S. J. Wind, Phys. Rev. B **45**, 11419 (1992).

[17] B. W. Alphenaar, A. A. M. Staring, H. van Houten, M. A. A. Mabesoone, O. J. A. Buyk, and C. T. Foxon, Phys. Rev. B **46**, 7236 (1992).

[18] A. A. M. Staring, B. W. Alphenaar, H. van Houten, L. W. Molenkamp, O. J. A. Buyk, M. A. A. Mabesoone, and C. T. Foxon, Phys. Rev. B **46**, 12869 (1992).

[19] T. Heinzel, D. A. Wharam, J. P. Kotthaus, G. Böhm, W. Klein, G. Tränkle, and G. Weimann, Phys. Rev. B **50**, 15113 (1994).

[20] N. C. van der Vaart, M. P. de Ruyter van Steveninck, L. P. Kouwenhoven, A. T. Johnson, Y. V. Nazarov, C. J. P. M. Harmans, and C. T. Foxon, Phys. Rev. Lett. **73**, 320 (1994).

[21] O. Klein, C. de C. Chamon, D. Tang, D. M. Abusch-Magder, U. Meirav, X. G. Wen, M. A. Kastner, and S. J. Wind, Phys. Rev. Lett. **74**, 785 (1995).

[22] N. C. van der Vaart, L. P. Kouwenhoven, M. P. de Ruyter van Steveninck, Y. V. Nazarov, C. J. P. M. Harmans, and C. T. Foxon, Phys. Rev. B **55**, 9746 (1997).

[23] O. Astafiev, V. Antonov, T. Kutsuwa, and S. Komiyama, Phys. Rev. B **62**, 16731 (2000).

[24] F. E. Camino, W. Zhou, and V. J. Goldman, Phys. Rev. Lett. **95**, 246802 (2005).

[25] F. E. Camino, W. Zhou, and V. J. Goldman, Phys. Rev. B **72**, 155313 (2005).

[26] C. J. B. Ford, P. J. Simpson, I. Zailer, D. R. Mace, M. Yosefin, M. Pepper, D. A. Ritchie, J. E. F. Frost, M. P. Grimshaw, and G. A. C. Jones, Phys. Rev. B **49**, 17456 (1994).

[27] S. W. Hwang, J. A. Simmons, D. C. Tsui, and M. Shayegan, Phys. Rev. B **44**, 13497 (1991).

[28] G. Kirczenow, A. S. Sachrajda, Y. Feng, R. P. Taylor, L. Henning, J. Wang, P. Zawadzki, and P. T. Coleridge, Phys. Rev. Lett. **72**, 2069 (1994).

[29] D. R. Mace, C. H. W. Barnes, G. Faini, D. Mailly, M. Y. Simmons, C. J. B. Ford, and M. Pepper, Phys. Rev. B **52**, R8672 (1995).

[30] A. S. Sachrajda, Y. Feng, R. P. Taylor, G. Kirczenow, L. Henning, J. Wang, P. Zawadzki, and P. T. Coleridge, Phys. Rev. B **50**, 10856 (1994).

[31] B. L. Johnson, A. S. Sachrajda, G. Kirczenow, Y. Feng, R. P. Taylor, L. Henning, J. Wang, P. Zawadzki, and P. T. Coleridge, Phys. Rev. B **51**, 7650 (1995).

[32] I. J. Maasilta and V. J. Goldman, Phys. Rev. B **57**, R4273 (1998).

[33] C. Gould, A. S. Sachrajda, M. W. C. Dharma-wardana, Y. Feng, and P. T. Coleridge, Phys. Rev. Lett. **77**, 5272 (1996).

[34] M. Kataoka, C. J. B. Ford, M. Y. Simmons, and D. A. Ritchie, Phys. Rev. Lett. **89**, 226803 (2002).

[35] M. Kataoka, C. J. B. Ford, G. Faini, D. Mailly, M. Y. Simmons, D. R. Mace, C.-T. Liang, and D. A. Ritchie, Phys. Rev. Lett. **83**, 160 (1999).

[36] B. Rosenow and B. I. Halperin, Phys. Rev. Lett. **98**, 106801 (2007).

[37] P.-A. Huynh, F. Portier, H. le Sueur, G. Faini, U. Gennser, D. Mailly, F. Pierre, W. Wegscheider, and P. Roche, Phys. Rev. Lett. **108**, 256802 (2012).

[38] C. A. Stafford and S. Das Sarma, Phys. Rev. Lett. **72**, 3590 (1994).

[39] L. P. Kouwenhoven, F. W. J. Hekking, B. J. van Wees, C. J. P. M. Harmans, C. E. Timmering, and C. T. Foxon, Phys. Rev. Lett. **65**, 361 (1990).

[40] F. R. Waugh, M. J. Berry, D. J. Mar, R. M. Westervelt, K. L. Campman, and A. C. Gossard, Phys. Rev. Lett. **75**, 705 (1995).

[41] W.-Y. Wei, T.-S. Lo, C.-C. Tang, K.-T. Lin, M. Brink, D.-C. Ling, C.-C. Chi, C.-Y. Mou, J.-C. Chen, D. M. Newns, and C. C. Tsuei, arXiv:1603.04625.

[42] W. G. van der Wiel, S. De Franceschi, J. M. Elzerman, T. Fujisawa, S. Tarucha, and L. P. Kouwenhoven, Rev. Mod. Phys. **75**, 1 (2002).

[43] Y. Zhang, D. T. McClure, E. M. Levenson-Falk, C. M. Marcus, L. N. Pfeiffer, and K. W. West, Phys. Rev. B **79**, 241304 (2009).

[44] Y. Meir, N. S. Wingreen, and P. A. Lee, Phys. Rev. Lett. **66**, 3048 (1991).

[45] T. Byrnes, N. Y. Kim, K. Kusudo, and Y. Yamamoto, Phys. Rev. B **78**, 075320 (2008).

[46] S. Datta, *Electronic Transport in Mesoscopic Systems* (Cambridge University Press, Cambridge, 1997).

[47] Y. V. Nazarov and Y. M. Blanter, *Quantum Transport: Introduction to Nanoscience* (Cambridge University Press, Cambridge, 2009).